Optimized signal deduction procedure for the MIEZE neutron spectroscopy technique

J. K. Jochum

Heinz Maier-Leibnitz Zentrum (MLZ), Technische Universität München, D-85748 Garching, Germany

L. Spitz

Heinz Maier-Leibnitz Zentrum (MLZ), Technische Universität München, D-85748 Garching, Germany

C. Franz

Heinz Maier-Leibnitz Zentrum (MLZ), Technische Universität München, D-85748 Garching, Germany
Physik Department, Technische Universität München, D-85748 Garching, Germany
Jülich Centre for Neutron Science JCNS-MLZ, Forschungszentrum Jülich GmbH Outstation at MLZ FRM-II, 85747 Garching, Germany

J. C. Leiner

Physik Department, Technische Universität München, D-85748 Garching, Germany

C. Pfleiderer

Physik Department, Technische Universität München, D-85748 Garching, Germany

O. Soltwedel

Physik Department, Technische Universität München, D-85748 Garching, Germany
Institut für Physik Kondensierter Materie, Technische Universität Darmstadt, D-64289 Darmstadt, Germany

E-mail: soltwedel@fkp.tu-darmstadt.de

Abstract. We report a method to determine the phase and amplitude of sinusoidally modulated event rates, binned into 4 bins per oscillation. The presented algorithm relies on a reconstruction of the unknown parameters. It omits a calculation intensive fitting procedure and avoids contrast reduction due to averaging effects. It allows the current data acquisition bottleneck to be relaxed by a factor of 4. Here, we explain the approach in detail and compare it to the established fitting procedures of time series having 4 and 16 time bins per oscillation. In addition we present the empirical estimates of the errors of the three methods and compare them to each other. We show that the reconstruction is unbiased, asymptotic, and efficient for estimating the phase. Reconstructing the contrast, which corresponds to the amplitude of the modulation, is roughly 10% less efficient than fitting 16 time binned oscillations. Finally, we give analytical equations to estimate the error for phase and contrast as a function of their initial values and counting statistics.

PACS numbers: keywords: neutron spectroscopy, neutron resonance spin-echo, mieze, error estimation

1. Introduction

MIEZE (Modulation of IntEnsity with Zero Effort) spectroscopy is a hybrid technique combining neutron resonance spin-echo (NRSE) and neutron Time-of-Flight (ToF) spectroscopy. It is routinely available at the NRSE-Spectrometer RESEDA at the Heinz Maier-Leibnitz Zentrum [1]. In Fig. 1 we present a basic MIEZE set-up. It uses neutron spin precession generated by two resonant (neutron) spin flippers (RSF_1 and RSF_2) separated by a distance L_1 and operated at individual frequencies ($f_1 < f_2$), to manipulate the spin eigenstates [2, 3]. The resulting interference pattern of the superposition of the spin states corresponds to a sinusoidal intensity as a function of time akin an optical heterodyne interferometer.

Also, in MIEZE, the modulation frequency of the intensity is given by twice the difference of the RSF frequencies $f_{\mathrm{MIEZE}} = 2(f_2 - f_1)$. The coherence volume of the interference is indirectly proportional to the wavelength of the incoming neutron beam, the width of the wavelength band, and f_{MIEZE} [4, 5]. Its center is located at a point L_2 downstream RSF_2. It is exclusively determined by the frequency ratio and distance of both flippers $\frac{f_2-f_1}{f_1} = \frac{L_1}{L_2}$ [6]. In practice these frequencies are limited at the lower end by the neutron spin flip efficiency generated by the Bloch-Siegert-shift to $f_{\mathrm{min}} = 35\,\mathrm{kHz}$ [7]. The limitations at the upper end are due to skin and proximity effects in the resonant flippers, as well as parasitic capacities in the resonant circuits, which currently sets the maximum RSF frequency to $f_{\mathrm{max}} = 3.6\,\mathrm{MHz}$ [8, 3]. Without loss of generality, the experimental description given here includes only those components necessary to produce the intensity as modulated in time. Further details and a description of the MIEZE setup may be found in Refs. [9, 10].

In contrast to conventional neutron spin-echo (NSE), the quantity measured in MIEZE corresponds to a sinusoidally modulated intensity in time. From a practical point of view the detector registers events per oscillation and histograms according to a certain number of time bins [11]. Thus, for a fixed number of time bins, the length of each time bin is a function of the modulation frequency. The lower limit of the time bin length is given naturally by the temporal resolution of the detector, which is limited by the electron drift time and the clock of the electronics readout of the detector [11]. Hence, to detect signals with fast modulation, it is necessary for the number of time bins to be as low as possible. In contrast, an insufficient number of time bins per oscillation results in a smearing of the recorded oscillation amplitude.

Without loss of generality and neglecting the average background count rate, the event rate registered by a detector recording signals at discrete intervals in time is given by the integral over a harmonic oscillation with amplitude I_0 and arbitrary phase ϕ_0

$$I' = \frac{I_0}{\Delta\phi} \int_{-\frac{\Delta\phi}{2}}^{\frac{\Delta\phi}{2}} \sin(\phi - \phi_0)\, d\phi \tag{1a}$$

$$I' = I_0 \sin(\phi_0) \frac{\sin\frac{\Delta\phi}{2}}{\frac{\Delta\phi}{2}}. \tag{1b}$$

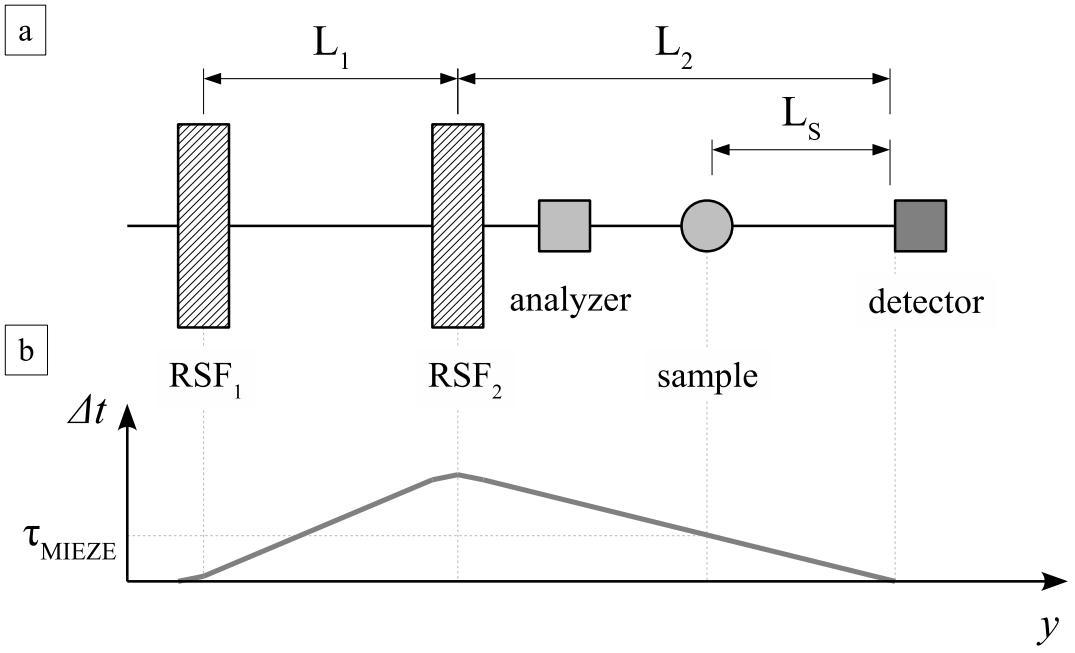

Figure 1. (a) Schematic representation of the essential parts of the MIEZE setup. Polarized neutrons travel in the y-direction passing the resonant spin flippers (RSF_1 and RSF_2) and the precession region between them, the spin analyser, the sample, and finally hitting the detector. (b) The time-of-flight difference Δt of the spin eigenstates as function of distance along the flight path is shown. The time-of-flight difference at the sample position is τ_{MIEZE}

where $\Delta\phi = \frac{2\pi}{\#\,timebins}$. In this resolution function the sinc-function acts as a damping factor, which assumes a minimum value if $\Delta\phi = 0$, i.e. infinite time bins representing a trivial but prohibitively impractical solution. Keeping in mind that at least three parameters I_{mean} (the time average), I_0 (the amplitude), and ϕ_0 (the arbitrary phase) must be extracted from the signal, a minimum of three time bins is necessary for an unambiguous reconstruction. From this the MIEZE contrast $C = \frac{I_0}{I_{\mathrm{mean}}}$ may be extracted [6].

A good compromise between the number of time bins and the magnitude of the reduction factor are 16 time bins, the default value for MIEZE experiments at RESEDA. In this regime, the damping induced by the sinc-function is only 0.64%. Currently a detector with a clock rate of 10 MHz is used to detect the MIEZE-signals at RESEDA [11]. Therefore, the maximum MIEZE frequency is limited to $f_{\mathrm{MIEZE}} = \frac{10\,\mathrm{MHz}}{16} = 625\,\mathrm{kHz}$ when using 16 time bins. In order to increase the resolution (e.g. τ_{MIEZE}, the Fourier time), f_{MIEZE} has to be maximized since it is directly proportional to τ_{MIEZE} by the following equation

$$\tau_{\mathrm{MIEZE}} = \frac{2\pi\,\hbar\,L_{\mathrm{S}}}{m_{\mathrm{n}} v_{\mathrm{n}}^3}\, f_{\mathrm{MIEZE}} \tag{2}$$

with the neutron mass m_{n}, its velocity v_n, and the sample detector distance L_{S} (cf. Fig. 1).

A practical solution is to reduce the number of time bins, fit the points with a sine function, and stretch the amplitude by normalizing it to the damping factor given by (1a). Since the measurements are normalized to the instrumental resolution function (which depends equally on the damping factor), the damping factor cancels out, and therefore does not need to be taken into account explicitly. Alternatively, one may find an unbiased estimate to reconstruct the fitting parameters from the minimum necessary time bins by taking the time integration of the detector into account. In the following sections, a reconstruction procedure of the underlying parameters will be deduced using only four time bins. This relaxes the data acquisition by a factor of 4 corresponding to $f^{\max}_{\mathrm{MIEZE}} = 2.5\,\mathrm{MHz}$. Although three time bins are the optimal choice to cover the highest frequencies, we focus here on four time bins because of their backwards compatibility with older data sets histogrammed in 16 time bins. In turn, all data recorded at RESEDA previously may be evenly merged into 4 time bins for direct comparisons.

2. Reconstruction of the MIEZE Signal

As starting point for the reconstruction of the MIEZE signal, we give the mathematical description of the time dependent event rate $I(t)$ as recorded by the detector. This signal may be split into a time-dependent and a time-independent contribution (I_{mean}). The latter describes the intrinsic background and all of the contrast reductions such as incoherent scattering, spin leakage, and sample dynamics. The sinusoidal time-dependence is characterized by the amplitude I_0, the duration $T = \frac{1}{f_{\mathrm{MIEZE}}}$, and phase shift ϕ_0. These combine to give $I(t)$ as

$$I(t) \;=\; I_{\mathrm{mean}} \;+\; I_0 \,\sin\left(\frac{2\pi}{T}t - \phi_0\right). \tag{3}$$

Since the time binning of events in the detector is equal to an integration over time of $I(t)$ in the respective interval, one may write the number of detected events in the k^{th} interval I_{k} as

$$I_k \;=\; \frac{1}{T}\int_{\frac{\mathrm{T}}{\mathrm{N}}(\mathrm{k}-1)}^{\frac{T}{N}k} I(t)dt. \tag{4}$$

with $k = 1, 2, 3, ..., N$ for N bins. Normalizing I_{k} by I_{mean} corresponds to the probability of a single event occurring in the k^{th} interval. This fact will be employed later to mimic the discrete time events I_k in a simulation.

For a subdivision into four intervals ($N = 4$ cf. Fig. 2 gray shaded area for I_1) one

may rewrite (4) as follows

$$I_1 = \frac{I_{\text{mean}}}{4} + \frac{I_0}{2\pi}\left(\sin(-\phi_0) + \cos(-\phi_0)\right), \tag{5a}$$

$$I_2 = \frac{I_{\text{mean}}}{4} + \frac{I_0}{2\pi}\left(\cos(-\phi_0) - \sin(-\phi_0)\right), \tag{5b}$$

$$I_3 = \frac{I_{\text{mean}}}{4} + \frac{I_0}{2\pi}\left(-\sin(-\phi_0) - \cos(-\phi_0)\right), \tag{5c}$$

$$I_4 = \frac{I_{\text{mean}}}{4} + \frac{I_0}{2\pi}\left(-\cos(-\phi_0) + \sin(-\phi_0)\right). \tag{5d}$$

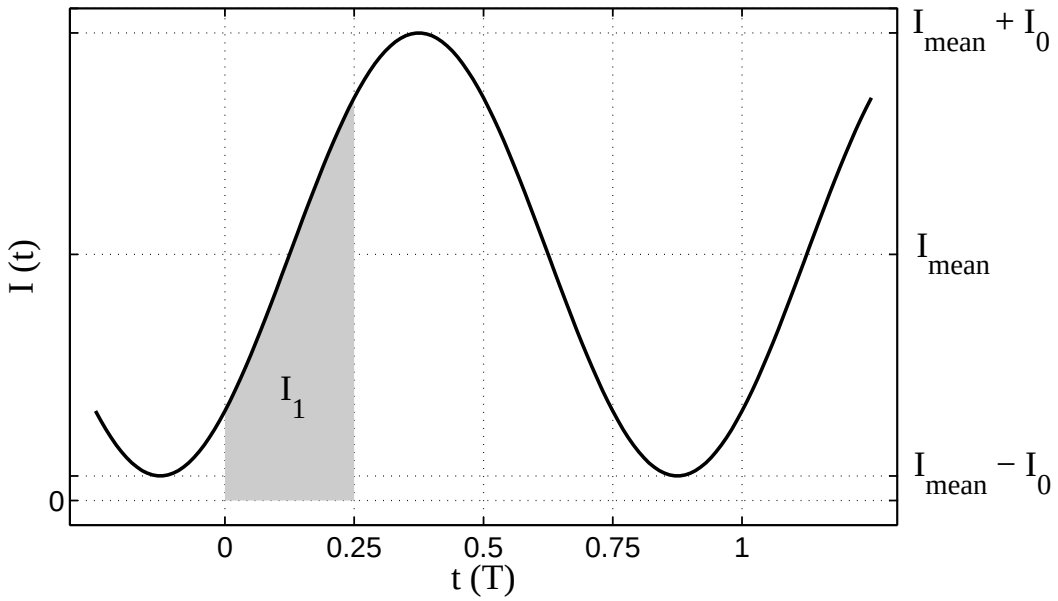

Figure 2. A typical time-dependent sinusoidal intensity variation with phase $\phi_0 = \frac{\pi}{8}$ and a contrast $C = \frac{I_0}{I_{\text{mean}}}$ that is defined by the amplitude I_0 and the mean value I_{mean}. The gray shaded area I_1 normalized to I_{mean} is the probability of a single event being detected in the first interval from the division of each oscillation of $I(t)$ into four equally long time bins.

Summing up neighbouring intervals and simplifying the results yields

$$I_1 + I_2 = \frac{I_{\text{mean}}}{2} + \frac{I_0}{\pi}\cos(-\phi_0) \tag{6a}$$

$$I_2 + I_3 = \frac{I_{\text{mean}}}{2} - \frac{I_0}{\pi}\sin(-\phi_0) \tag{6b}$$

$$I_3 + I_4 = \frac{I_{\text{mean}}}{2} - \frac{I_0}{\pi}\cos(-\phi_0) \tag{6c}$$

$$I_4 + I_1 = \frac{I_{\text{mean}}}{2} + \frac{I_0}{\pi}\sin(-\phi_0). \tag{6d}$$

Adding the next nearest neighbour intervals ($I_1 + I_3$ as well as $I_2 + I_4$) yields only the direct component (first terms) while the phase information is lost. This is a direct consequence of the signal's harmonic periodicity.

Since the equations (6a) - (6d) are sums of neighbouring intervals, one may use two independent but identical detector read outs $\frac{\pi}{2}$ phase shifted of two time intervals each to reach the same result. In doing so one doubles $f^{\max}_{\mathrm{MIEZE}}$.

In analogy to the well established quadrature detection in optical interferometers [12], the equations (6a) - (6d) may be combined to yield the reconstructed phase $\phi_{0,\mathrm{rec}}$

$$\tan(-\phi_{0,\mathrm{rec}}) = \frac{I_4 + I_1 - (I_2 + I_3)}{I_1 + I_2 - (I_3 + I_4)}. \tag{7}$$

It is also possible to deduce the phase by subtracting equations (5a) - (5d) from each other.

$$\frac{I_1 - I_2}{I_1 - I_4} = \tan(-\phi_0) \tag{8a}$$
$$\frac{I_1 - I_2}{I_2 - I_3} = \tan(-\phi_0) \tag{8b}$$
$$\frac{I_4 - I_3}{I_1 - I_4} = \tan(-\phi_0) \tag{8c}$$
$$\frac{I_4 - I_3}{I_2 - I_3} = \tan(-\phi_0) \tag{8d}$$

These equations show that one interval can be neglected. However, for this approach information in form of counts is ignored within the respective interval, thus reducing the overall statistic and accuracy. Indeed, upon closer inspection, the average over equations (8a) - (8d) equals equation (7), a fact confirmed by simulations.

Based on the calculations presented below the phase, the contrast may be deduced as well. To do so, the aforementioned relation $C = \frac{I_0}{I_{\mathrm{mean}}}$ is used, where I_0 is extracted by combining either equations (6a) and (6c) or (6b) and (6d).

$$C_{1,\mathrm{rec}} = \frac{I_1 + I_2 - (I_3 + I_4)}{I_1 + I_2 + I_3 + I_4} \cdot \frac{\pi}{2\cos\phi_{0,\mathrm{rec}}} \tag{9a}$$
$$C_{2,\mathrm{rec}} = \frac{I_1 + I_4 - (I_2 + I_3)}{I_1 + I_2 + I_3 + I_4} \cdot \frac{\pi}{2\sin\phi_{0,\mathrm{rec}}} \tag{9b}$$

Of course the accuracy of the evaluated contrast is strongly coupled to the accuracy of the estimated phase and diverges at the singularities, i.e., when $\cos\phi_{0,\mathrm{rec}}$ or $\sin\phi_{0,\mathrm{rec}}$ tend towards zero. In order to avoid the singularities we apply equations (9a) and (9b)

for the appropriate case.

$$C_{\mathrm{rec}} = \begin{cases} C_{1,\mathrm{rec}}, & \text{for } \cos\phi_{0,\mathrm{rec}} \geq \sin\phi_{0,\mathrm{rec}} \\ C_{2,\mathrm{rec}}, & \text{for } \cos\phi_{0,\mathrm{rec}} < \sin\phi_{0,\mathrm{rec}} \end{cases} \tag{10}$$

3. Estimation of the confidence interval

Next, we discuss how many events are necessary to determine phase and contrast with a desired accuracy. As a first attempt, these uncertainties are estimated using Gaussian error propagation with the relative errors $\frac{1}{\sqrt{I_k}}$. Deducing the partial derivatives is straightforward. Less obvious is the estimate of the total errors $\Delta I_1, ... I_4$, due to their mutual dependence. Moreover, the total errors also depend on C_0 and ϕ_0. At this point, it would be appropriate to use the generalized Gaussian error propagation, which accounts also for the covariance between all parameters.

To circumvent this multi-dimensional exercise, we applied simulations and executed them for various initial phases ($\phi_0 = 0°, 15°, ..., 120°$) and contrasts ($C_0 = 0.05, 0.1, ..., 0.95$). First 10 single events with the desired sinusoidal distribution are generated using the pseudo-random generator of MATLAB® (the code used was published in Ref. [13]) and histogrammed subsequently. For a given C_0 and ϕ_0, the probability to fall in a certain time bin is determined by equations (5a) - (5d). Subsequently, the phase and contrast are calculated according to the reconstruction method and the standard fit over 4 and 16 time bins for the same data set. Next, new events are added to this time series and the evaluation is repeated recursively.

The number of added events in such a series increases logarithmically. This ensures a low computational burden over a large dynamic range of events (here over five orders of magnitude) and keeps the evaluation equally weighted in a logarithmic representation. Finally, the results are compared with each other (cf. Fig. 3 (a) and (d)). It is found that the phases estimated for the 4 point fitting method (red) and the reconstruction (green) are of high accuracy identical when there are more than 30 events.

For a low number (< 30) of events, the phase and contrast values have larger deviations from the true values as the result of insufficient statistics. As expected from equation (1b), both fitting methods show biased contrast estimates. For the contrast $C_0 = 0.85$ presented in Fig. 3, the expected deviations according to equation. (1b) are $0.64\% \cdot C_0 = 0.0054$ for the 16 time bins (blue) and $10\% \cdot C_0 = 0.085$ for 4 time bins (green). This allows for a comparison of the contrasts measured under different binning conditions. It also shows that the estimates inferred from the reconstruction method are unbiased.

It should be emphasized that in a real measurement, the contrasts detected experimentally are normalized by a resolution function determined under the same conditions. Therefore, the errors occurring from unbiased estimators would cancel out if the same estimator is used for treating resolution and measurement data.

To estimate the standard deviations of the phase and the contrast, the simulation

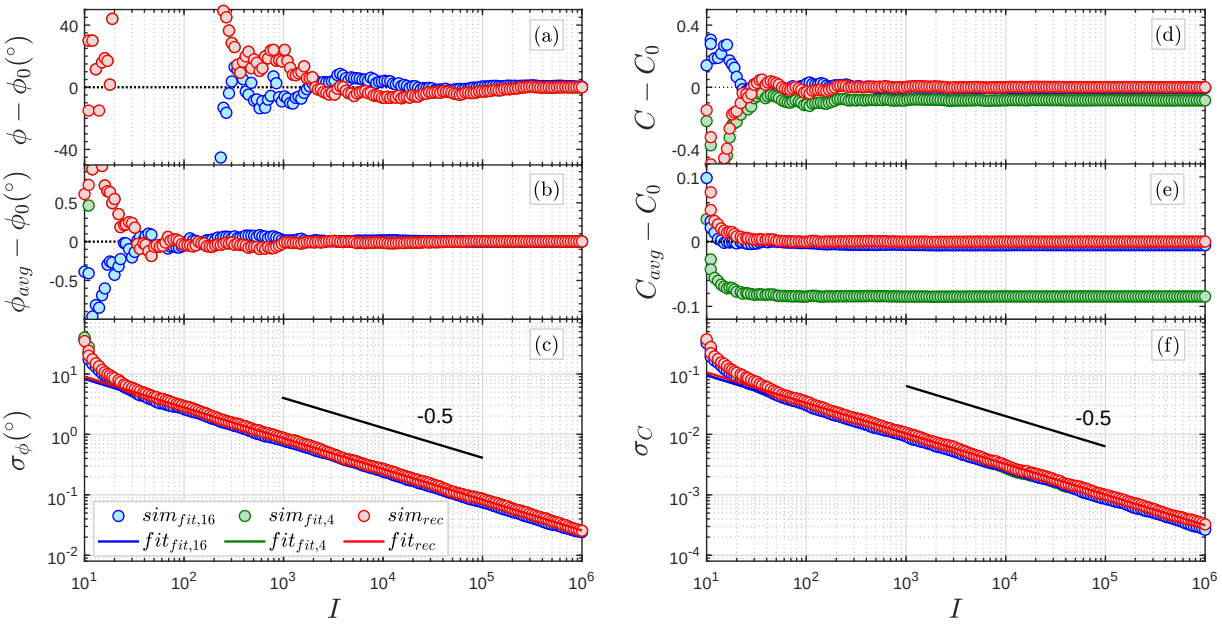

Figure 3. For the initial parameters $C_0 = 0.85$, $\phi_0 = 60°$, approximated deviations for phase ϕ ((*a*),(*b*),(*c*)) and contrast C ((*d*),(*e*),(*f*)) versus the number of total count events ($I = I_1 + I_2 + ... + I_k$) for a single time series ((*a*) and (*d*)) and averaged over 500 time series ((*b*) and (*e*)). The standard deviations ((*c*) and (*f*)) calculated respectively for the reconstruction method (red) and generic fitting procedures using 4 (green) and 16 (blue) time bins are displayed as dots together with their fits (solid lines). As a guide to the eye, the black lines show a power law with an exponent of -0.5. To highlight the significance of the resulting phase as a function of events, (*a*) and (*d*) have been purposefully cropped. Except for Fig. 3 (*d*) and (*e*), the green data points coincide with the red data points reflecting nearly identical values.

was repeated 500 times in order to sample a large number of values from the random-number generator. From these data, the average phase (ϕ_{avg}) and contrast (C_{avg}) as well as their corresponding standard deviations (σ_ϕ and σ_{C}) were calculated as a function of events I (cf. Fig. 3 (b), (c), (e) and (f)). Again, while the average phase is estimated correctly, the unbiased estimate for the contrast bears the expected deviations. Interestingly though, the estimated standard deviations σ_ϕ and σ_{C} (for the reconstruction and fitting procedures) decrease with the same asymptotic behavior as the total number of events ($I = \sum_{\mathrm{k}}^{N} I_k$) increases (cf. Fig. 3 (c) and (f)). This proves that the procedure used here is asymptotically consistent.

Moreover, the relationship between standard deviation and events, for both the phase and contrast, is described by simple power laws

$$\sigma_\phi(I) = 10^{\beta_\phi} \cdot I^{\alpha_\phi}, \tag{11a}$$

$$\sigma_{\mathrm{C}}(I) = 10^{\beta_{\mathrm{C}}} \cdot I^{\alpha_{\mathrm{C}}}. \tag{11b}$$

From a linear fit to the log-log plot of the estimated standard deviations (c.f. Fig. 3 panels (c) and (f)) for more than 30 events, the power law exponents (α_ϕ and α_{C}) may

be inferred

$$\alpha_\phi = \alpha_\mathrm{C} \approx -0.5. \tag{12}$$

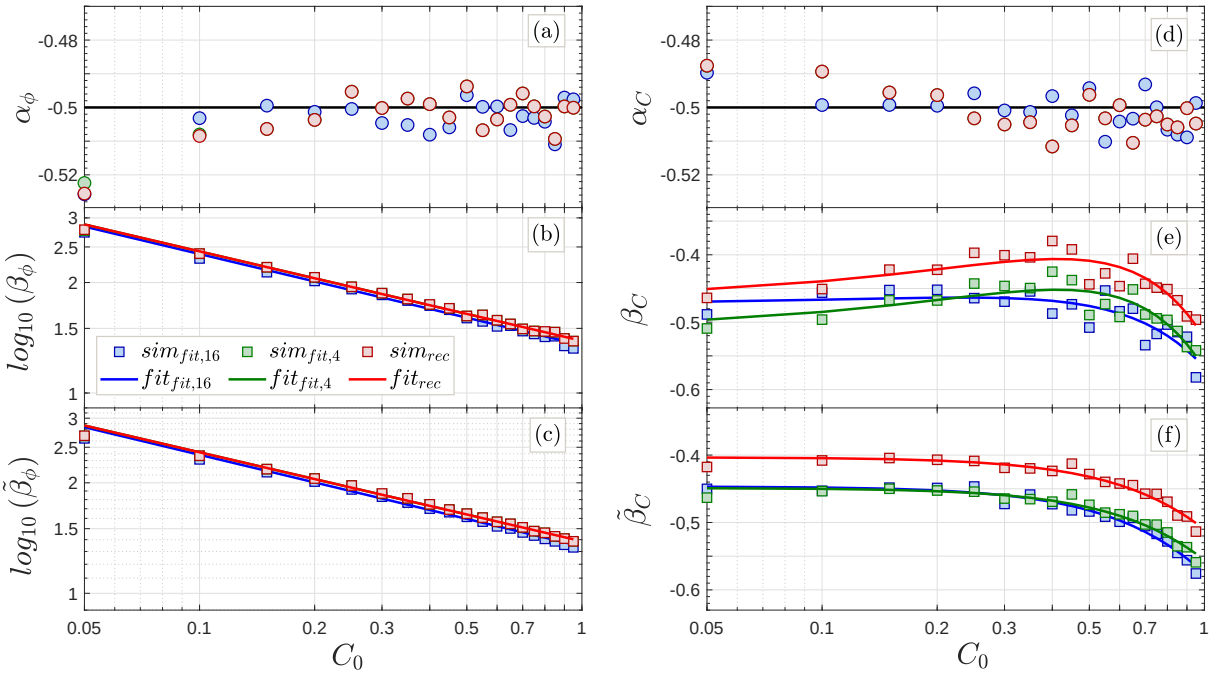

Figure 4. Fit parameter of the error estimation for phase (α_ϕ (a) and β_ϕ (b)) and contrast (α_C (d) and β_C (e)) as a function of the initial contrast C_0 and a fixed phase $\phi_0 = 60°$. Panels (c) and (f) show the scaling parameters $\tilde{\beta}_\phi$ and $\tilde{\beta}_C$ using the constraint $\alpha_* = -0.5$. The color code is the same as for Fig. 3. Apart from plots (e) and (f), the values deduced from 4-point-fit and reconstruction method overlap each other.

To test the generality of this power law behavior and to determine the missing parameters (β_ϕ and β_C) for varying contrasts, the simulations for $C_0 = 0.05, 0.1, ..., 0.95$ were repeated while keeping the initial phase fixed $\phi_0 = 60°$. In Fig. 4, parameters of the reconstruction and fitting methods are deduced for a comprehensive range of representative contrasts. For each such contrast (C_0), α_ϕ and α_C (cf. 4 (a) and (d)) remain nearly unchanged, confirming that use of a normal distribution to approximate a Poisson distribution is well justified. Further, the coefficients β_ϕ and β_C show quantitatively distinct dependencies on the initial parameter C_0 (cf. Fig. 4 (b) and (e)). The phase was observed to follow an exponential decay with increasing C_0

$$\beta_\phi = \beta_{2,\phi} C_0^{\beta_{1,\phi}}. \tag{13}$$

with decay constants $\beta_{2,\phi}$ and $\beta_{1,\phi}$ which vary slightly depending on the method. The functional dependence of the contrast is less obvious, and the parabolic fits (solid lines) in Fig. 4 (e) are not-optimal.

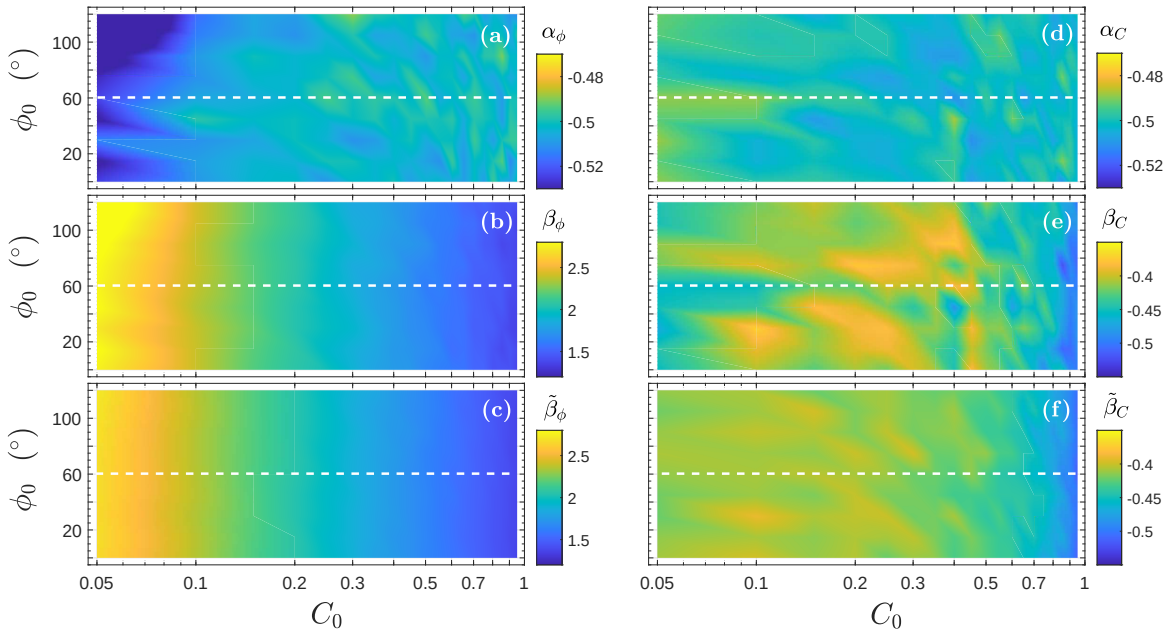

Figure 5. Color-map plots of parameters α_ϕ (a), β_ϕ (b), α_C (d), β_C (e) for varying initial phases ϕ_0 and contrasts C_0 using the reconstruction. All four parameters are nearly independent of the initial phase ϕ_0. While the parameters (α_ϕ and α_C) remain nearly constant even through varying initial contrasts, β_ϕ decays exponentially with increasing contrast. Analogously to Fig. 4 (e) β_C shows a nonphysical trend with a maximum at $C_0 \approx 0.4$. Panels (c) and (f) show the scaling parameters $\tilde{\beta}_\phi$ and $\tilde{\beta}_C$ using the constraint $\alpha_* = -0.5$.

Since α_* and β_* ($* = \phi$ or C.) depend on each other, as the fits are overparameterized, β_* was recalculated with the constraint $\alpha_* = -0.5$. For the sake of clarity, β_* is renamed $\tilde{\beta}_*$ in the following if the constraint ($\alpha_* = -0.5$) is applied. The resulting fits are plotted in Figs. 4 (c) and (f). Compared to Fig. 4 (b), the exponential dependence of $\tilde{\beta}_\phi$ is maintained. Furthermore, $\tilde{\beta}_C$ can now be described well by a shifted half-normal distribution

$$\tilde{\beta}_C = \beta_{2,C} \cdot e^{-\left(\frac{C_0}{\beta_{1,C}}\right)^2} - 1. \tag{14}$$

To show that these findings hold for the relevant range of phases, this procedure was repeated for $\phi_0 = (0 \ldots 120°)$ in steps of 15°. This yields a set of curves comparable to the ones in Fig. 4, which are color-plotted in Fig. 5, highlighting their behavior throughout the entire parameter space. The plots confirm that the fitting parameters deduced with these techniques are practically independent of ϕ_0. One may note that due to the periodicity of the harmonic functions, these findings are valid for all phases.

Combining equations 11a, 11b, 13, and 14, the analytical equations for an estimate

of the standard deviation may be defined as

$$\sigma_\phi \;=\; 10^{\left(\beta_{2,\phi}\cdot C_0^{\beta_{1,\phi}}\right)} \;\cdot\; \frac{1}{\sqrt{I}}, \tag{15a}$$

$$\sigma_{\mathrm{C}} \;=\; 10^{\left(\beta_{2,\mathrm{C}}\cdot e^{-\left(\frac{C_0}{\beta_{1,C}}\right)^2}-1\right)} \;\cdot\; \frac{1}{\sqrt{I}}. \tag{15b}$$

Typical method dependent parameter values are summarized in Table 1.

Table 1. Parameters to deduce the standard deviations σ_ϕ and σ_C using equations 15a and 15b, for the reconstruction and 4- and 16-point fitting methods.

method	$\beta_{1,\phi}$	$\beta_{2,\phi}$	$\beta_{1,C}$	$\beta_{2,C}$
reconstruction	-0.244	1.383	2.29	0.60
4-point-fit	-0.244	1.341	7.90	0.95
16-point-fit	-0.250	1.383	9.15	0.95

4. Conclusions

We have presented an algorithm to deduce the contrast and the phase of a sinusoidally modulated time series sampled at four data points per oscillation. Both, contrast and phase are recovered in agreement with 16 time bins. The reconstruction trades in a higher time resolution for less accurate contrast. Quantitatively, this factor is better than $\frac{\sigma_{\mathrm{C0,fit,16}}}{\sigma_{\mathrm{C0,rec}}} \geq 0.9$ compared to the fitting method, but may be compensated by increased statistics, i.e around 20% prolonged counting time. However, using the reconstruction, there is no fitting procedure involved which significantly reduces the required computational burden. Thus, this method may be readily applied to a large number of detector pixels as the measurements proceed in time.

Most importantly, this new method solves one of the main limitations afflicting the MIEZE resolution. Using a CASCADE-type detector [11] with a maximum time resolution of 100 ns (10 MHz), the maximum intensity modulation frequency for 16 time channels is 625 kHz, which, at 6 Å with the current dimensions at RESEDA yields a MIEZE (Fourier) time of $\sim$3 ns. In stark juxtaposition, the resolution limit using the four-point method is $\sim$12 ns at 6 Å or $\sim$100 ns at 12 Å. However, for intensity modulation frequencies at or above 2.5 MHz, extremely flat detector surfaces are needed to minimize phase differences in a single pixel. A ^{10}B layer on a solid surface instead of Kapton foil could be a possible solution. Furthermore, a spherical detector foil shape would suppress the phase rings which occur on flat surfaces due to variations of path lengths. The only constraint towards achieving the highest resolution, or equivalently the highest MIEZE (Fourier) time, remains the undesired contributions of the sample's size and shape to the time-of-flight of individual neutrons [14, 15].

Finally, we would like to emphasize that the error bars deduced for the contrast using the 4 point fitting method must be treated carefully, since the procedure of inferring the estimate is biased. Re-scaling this contrast and its error with the damping factor of 0.9 given by (1a), the same error observed for the reconstruction method is maintained.

5. Acknowledgements

We wish to thank B. Pompe from University of Greifswald and T. Keller from Max-Planck-Institute for Solid State Research Stuttgart for very useful discussions and M. Klein from CDT GmbH for discussions and support of the CASCADE detector system. Financial support through the BMBF projects 'Longitudinale Resonante Neutronen Spin-Echo Spektroskopie mit Extremer Energie-Auflösung' (Förderkennzeichen 05K16W06) and 'Resonante Longitudinale MIASANS Spin-Echo Spektroskopie an RESEDA' (Förderkennzeichen 05K19W05) is gratefully acknowledged.

References

[1] C. Franz, T. Schröder, Reseda: Resonance spin echo spectrometer, Journal of large-scale research facilities 1 (14) (2015).

[2] R. Gähler, R. Golub, K. Habicht, T. Keller, J. Felber, Space-time description of neutron spin echo spectrometry, Physica B: Condensed Matter 229 (1) (1996) 1 – 17.

[3] J. K. Jochum, A. Hecht, O. Soltwedl, C. Fuchs, J. Frank, E. Faulhaber, J. C. Leiner, C. Pfleiderer, C. Franz, Oscillatory magnetic fields for neutron resonance spin-echo spectroscopy, Measurement Science and Technology (2020).

[4] J. Felber, R. Gähler, R. Golub, K. Prechtel, Coherence volumes and neutron scattering, Physica B: Condensed Matter 252 (1-2) (1998) 34–43.

[5] J. K. Jochum, A. Wendl, T. Keller, C. Franz, Neutron MIEZE spectroscopy with focal length tuning, Measurement Science and Technology 31 (3) (2019) 035902.

[6] R. Gähler, R. Golub, T. Keller, Neutron resonance spin echo-a new tool for high resolution spectroscopy, Physica B: Condensed Matter 180 (1992) 899–902.

[7] F. Bloch, A. Siegert, Magnetic resonance for nonrotating fields, Phys. Rev. 57 (1940) 522–527.

[8] F. Groitl, T. Keller, D. Quintero-Castro, K. Habicht, Neutron resonance spin-echo upgrade at the three-axis spectrometer flexx, Review of Scientific Instruments 86 (2) (2015) 025110.

[9] C. Franz, O. Soltwedel, C. Fuchs, S. Säubert, F. Haslbeck, A. Wendl, J. K. Jochum, P. Böni, C. Pfleiderer, The longitudinal neutron resonant spin echo spectrometer RESEDA, Nuclear Instruments and Methods in Physics Research Section A: Accelerators, Spectrometers, Detectors and Associated Equipment 939 (2019) 22 – 29.

[10] T. Oda, M. Hino, H. Endo, H. Seto, Y. Kawabata, Tuning neutron resonance spin-echo spectrometers with pulsed beams, Phys. Rev. Applied 14 (2020) 054032.

[11] M. Köhli, M. Klein, F. Allmendinger, A.-K. Perrevoort, T. Schröder, N. Martin, C. J. Schmidt, U. Schmidt, Cascade - a multi-layer boron-10 neutron detection system, Journal of Physics: Conference Series 746 (1) (2016) 012003.

[12] S. Rerucha, Z. Buchta, M. Sarbort, J. Lazar, O. Cip, Detection of interference phase by digital computation of quadrature signals in homodyne laser interferometry, Sensors 12 (10) (2012) 14095–14112. doi:10.3390/s121014095.
URL https://www.mdpi.com/1424-8220/12/10/14095

[13] J. K. Jochum, L. Spitz, C. Franz, J. Leiner, C. Pfleiderer, O. Soltwedel, MATLAB Code for the Manuscript: Optimized signal deduction procedure for the MIEZE neutron spectroscopy technique (03 2021). doi:10.6084/m9.figshare.14193116.

[14] G. Brandl, R. Georgii, W. Häussler, S. Mühlbauer, P. Böni, Large scales-long times: Adding high energy resolution to sans, Nuclear Instruments and Methods in Physics Research Section A: Accelerators, Spectrometers, Detectors and Associated Equipment 654 (1) (2011) 394 – 398.

[15] N. Martin, On the resolution of a mieze spectrometer, Nuclear Instruments and Methods in Physics Research Section A: Accelerators, Spectrometers, Detectors and Associated Equipment 882 (2018) 11–16.